



Cite as
Nano-Micro Lett.
(2025) 17:289

Received: 10 March 2025
Accepted: 14 May 2025
© The Author(s) 2025

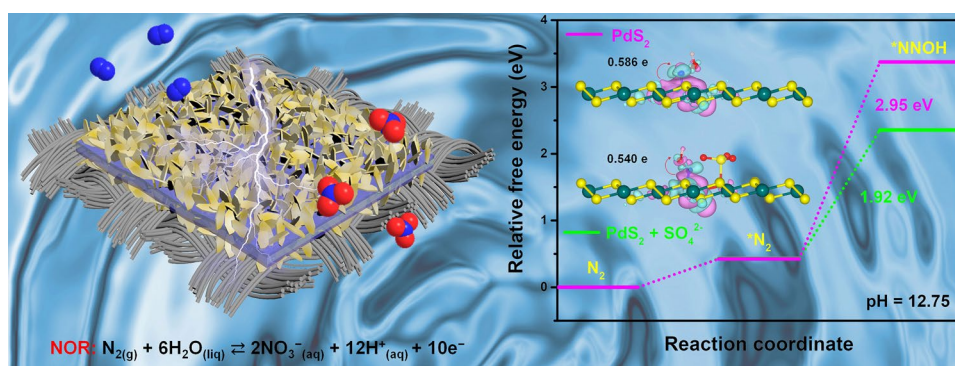
In Situ Generated Sulfate-Facilitated Efficient Nitrate Electrosynthesis on 2D PdS₂ with Unique Imitating Growth Feature

Rui Zhang^{1,2}, Hui Mao³ ✉, Ziyi Wang³, Shengke Ma³, Shuyao Wu³, Qiong Wu³, Daliang Liu³, Hui Li^{2,4}, Yang Fu^{2,4}, Xiaoning Li^{2,4}, Tianyi Ma^{2,4} ✉

HIGHLIGHTS

- Unique imitating growth feature for PdS₂ on different 2D substrates has been firstly discovered for constructing 2D/2D heterostructures by interface engineering.
- The thin and small PdS₂ nanoplates with active defects can be induced by poly(1-vinyl-3-ethylimidazolium bromide) (PVEIB), resulting in the obtained PdS₂@PVEIB/PPy/GO exhibited the excellent nitrogen oxidation reaction (NOR) electroactivity with the outstanding stability and selectivity.
- The in situ generation of SO₄²⁻, caused by the oxidation during the preparation process or exposed in air, as well as at high NOR potential, plays a crucial role in reducing the activation energy of the NOR process, leading to improved efficiency for nitrate production.

ABSTRACT As a green sustainable alternative technology, synthesizing nitrate by electrocatalytic nitrogen oxidation reaction (NOR) can replace the traditional energy-intensive Ostwald process. But low nitrogen fixation yields and poor selectivity due to the high bond energy of the N≡N bond and competition from the oxygen evolution reaction in the electrolyte restrict



its application. On the other hand, two-dimensional (2D) PdS₂ as a member in the family of group-10 novel transition metal dichalcogenides (NTMDs) presents the interesting optical and electronic properties due to its novel folded pentagonal structure, but few researches involve to its fabrication and application. Herein, unique imitating growth feature for PdS₂ on different 2D substrates has been firstly discovered

Rui Zhang and Hui Mao Contributed equally to this work.

✉ Hui Mao, huihao@lnu.edu.cn; Tianyi Ma, tianyi.ma@rmit.edu.au

¹ Shenyang Key Laboratory of Medical Molecular Theranostic Probes in School of Pharmacy, School of Pharmacy, Shenyang Medical College, Shenyang 110034, People's Republic of China

² Centre for Atomaterials and Nanomanufacturing (CAN), School of Science, RMIT University, Melbourne, VIC 3000, Australia

³ Institute of Clean Energy Chemistry, Liaoning Key Lab for Green Synthesis and Preparative Chemistry of Advanced Materials, College of Chemistry, Liaoning University, Shenyang 110036, People's Republic of China

⁴ ARC Industrial Transformation Research Hub for Intelligent Energy Efficiency in Future Protected Cropping (E2Crop), Melbourne, VIC 3000, Australia

Published online: 12 June 2025



SHANGHAI JIAO TONG UNIVERSITY PRESS

Springer

for constructing 2D/2D heterostructures by interface engineering. Due to the different exposed chemical groups on the substrates, PdS₂ grows as the imitation to the morphologies of the substrates and presents different thickness, size, shape and the degree of oxidation, resulting in the significant difference in the NOR activity and stability of the obtained composite catalysts. Especially, the thin and small PdS₂ nanoplates with more defects can be obtained by decorating poly(1-vinyl-3-ethylimidazolium bromide) on the 2D substrate, easily oxidized during the preparation process, resulting in the in situ generation of SO₄²⁻, which plays a crucial role in reducing the activation energy of the NOR process, leading to improved efficiency for nitrate production, verified by theoretical calculation. This research provides valuable insights for the development of novel electrocatalysts based on NTMDs for NOR and highlights the importance of interface engineering in enhancing catalytic performance.

KEYWORDS Imitating growth; PdS₂; Nanoplates; Nitrogen oxidation reaction (NOR); Synergistic effect

1 Introduction

With the increase in pressure of energy crisis and environmental pollution, more and more attentions have been attracted to the development of more sustainable alternatives to replace the traditional technologies based on renewable energy and green energy conversion technology [1–3]. Electrocatalysis is considered one of the most effective approaches to alleviate energy problems by using renewable energy-generated electricity to sustainably fuels or value-added chemicals [4–7]. Exploring stable and efficient electrocatalysts is the key to improve the rate of electrocatalysis, which has important strategic significance for the development of advanced energy conversion devices. Recently, electrocatalytic nitrogen oxidation reaction (NOR) has received extensive attentions, which involves the oxidation of N₂ on the electrode surface to produce nitrates or other nitrogen oxides; therefore, it is expected to become a green sustainable alternative technology for synthesizing nitrate under mild conditions, replacing the traditional Ostwald process with high energy consumption and large amounts of carbon dioxide emission [8–10]. The selection and design of the electrocatalysts are essential to NOR, because the activity, stability and selectivity of the catalyst can directly affect the efficiency of NOR and the quality of the product. Therefore, many attentions have been focused on developing efficient, stable and sustainable electrocatalysts to improve the NOR performance [11–13].

Recently, a breakthrough of improved NOR electroactivity has been achieved in FeS₂-TiO₂ heterogeneous nanoparticles or Pd²⁺/S²⁻-doped TiO₂ nanoparticles supported on 2-methylimidazolium functionalized polypyrrole/graphene oxide [14, 15]. Although the exact mechanism is not fully understood, it is believed that in these S-containing

materials, S²⁻ can be oxidized to persulfate reactive oxygen species (*SO₄) by *O generated during the competitive oxygen evolution reaction (OER) at high potentials, which then cooperatively activate nitrogen and further accelerate NOR [16]. Predictably, the improving NOR electroactivity would be potentially achieved by developing S-containing NOR electrocatalysts with preexisting *SO₄. Two-dimensional (2D) transition metal dichalcogenides (TMDs) possess unique electronic structure, large specific surface area and abundant surface/edge atoms, which can act as the promising electrocatalysts widely applied to water splitting and nitrogen fixation [17–19]. Many effective electrocatalysts based on 2D TMDs have been prepared for producing ammonia under ambient conditions by nitrogen reduction reaction (NRR); especially, the defect-rich 2D/2D heterostructures constructed by interface engineering exhibit improving catalytic activity and stability, because the crystal structure of 2D TMDs as the catalytic centers, such as MoS₂, can be adjusted and controlled by the specific inducing groups on the interface, generating the more defects exposed as the active sites [20–22]. Due to the existence of the defects, the surface/edge S²⁻ can be also easily converted to SO₄²⁻ by the oxidation, even during the synthesized process or exposed in the air, resulting in the preexistence of SO₄²⁻ in 2D TMDs. Therefore, 2D TMDs are expected as the ideal electrocatalysts for NOR in alkaline system, balancing NOR and OER to achieve optimal NO₃⁻ yield and Faraday efficiency (FE), even the excellent stability.

Different from the hexagonal structure in traditional TMDs, such as MoS₂ and WS₂, PdS₂ as a member in the family of group-10 novel TMDs (NTMDs) possesses a novel folded pentagonal structure, resulting in the interesting optical and electronic properties [23–25]. Up to now, the reports related to PdS₂ mostly have focused on theoretical

calculations [26–29], and few literatures involve to the fabrication and application of PdS₂, though PdS₂ exhibited high electroactivity in hydrogen evolution reactions (HER) process [30] and fuel cells [31]. Herein, unique imitating growth feature for 2D PdS₂ thin nanoplates on different 2D substrates has been firstly discovered and its electrocatalytic NOR performance can be significantly improved by the in situ generating *SO₄ from the oxidation of surface/edge S²⁻ due to the existence of active defects. Specifically, PdS₂ nanoplates can be anchored on the surfaces of graphene oxide (GO), polypyrrole/graphene oxide (PPy/GO) and poly(1-vinyl-3-ethylimidazolium bromide) functionalized polypyrrole/graphene oxide (PVEIB/PPy/GO) for constructing 2D/2D heterostructures by interface engineering. Caused by the different induction of the exposed chemical groups on the substrates, PdS₂ grows as the imitation to the morphologies of the substrates and present different thickness, size, shape and the degree of oxidation, resulting in the significant difference in the electrocatalytic NOR activity and stability of the obtained composite catalysts. The most excellent NOR performance with the significantly promoted stability can be achieved by PdS₂@PVEIB/PPy/GO among the obtained three 2D/2D heterostructures due to the synergistic effect of each component. Especially, the thin and small PdS₂ nanoplates with more defects can be obtained by the induction of PVEIB, easily oxidized during the preparation process or exposed in air, resulting in the in situ generation of SO₄²⁻, which plays a crucial role in reducing the activation energy of the NOR process, leading to improved efficiency for nitrate production, verified by both experimental and theoretical evidence. This research provides valuable insights for the development of novel electrocatalysts based on NTMDs for NOR and highlights the importance of interface engineering in enhancing catalytic performance.

2 Experimental Section

2.1 Preparation of Electrocatalysts Based on PdS₂

PdS₂ nanoplates were prepared by a simple hydrothermal process. In a typical experiment, K₂PdCl₆ (4.24 mL, 19.1 mg mL⁻¹) and thioacetamide (TAA, 113.4 mg) were dissolved in another 46 mL ultra-pure water, stirring for 10 min. Then, the mixture was transferred and sealed into a 100 mL of Teflon-lined stainless steel autoclave and

maintained at 200 °C for 24 h. Finally, the dark gray powders were collected and washed with ethanol and water by centrifugation and then dried in vacuum at 50 °C for 24 h. PdS₂@GO, PdS₂@PPy/GO and PdS₂@PVEIB/PPy/GO were also prepared by adjusting the content of precursor under the same conditions with different substrates. The used chemical reagents, preparation methods of the substrates, characterizations and apparatus were shown in the Supporting Information in detail.

2.2 Preparation of the Working Electrode for NOR

Separately selecting the pure PdS₂ nanoplates, PdS₂@GO, PdS₂@PPy/GO and PdS₂@PVEIB/PPy/GO as the electrocatalysts, the electrocatalysts suspension was prepared by adding 1.5 mg of electrocatalysts into 460 μL ethanol mixed with 40 μL Nafion perfluorinated resin solution, and ultrasound dispersed evenly for 30 min. A working electrode was constructed by dropping the above catalyst suspension onto a carbon cloth (CC) with area of 1.0 cm × 1.0 cm, used for conducting chronoamperometric measurement. The mass of electrocatalysts coating on CC was calculated by weighing after dried at 50 °C for 12 h.

2.3 Electrochemical Measurements and Nitrate Detection

The electrochemical performance of electrocatalysts based on PdS₂ was investigated by chronoamperometry with a CHI1040C Electrochemical Station (Shanghai CHENHUA Instrument Co., Ltd.). All the measurements were performed in 0.1 M KOH (pH = 12.75) containing saturated Ar or N₂ at room temperature. The chronoamperometry tests for detecting NO₃⁻ were performed in 50 mL of 0.1 M KOH solution in a standard three-electrode system using electrocatalysts coated on CC as the working electrode, a platinum plate as the counter electrode and a Hg/HgO electrode as the reference electrode. The measured potentials versus Hg/HgO were converted to reversible hydrogen electrode (RHE) scale according to the Nernst equation ($E_{\text{RHE}} = E_{\text{Hg/HgO}} + 0.059\text{pH} + 0.098$).

The produced NO₃⁻ was determined by an ion chromatography (IC). The standard curves and the calculation processes were shown in the Supporting Information in detail.

2.4 Electrochemical In Situ ATR-SEIRAS and Computational Method

The NOR mechanism was deduced through density functional theory (DFT) calculations, based on these detected N-containing oxide species measured by electrochemical in situ attenuated total reflection surface-enhanced infrared absorption spectroscopy (ATR-SEIRAS). The parameters of both electrochemical in situ ATR-SEIRAS and DFT calculations were shown in the Supporting Information in detail.

3 Results and Discussion

3.1 Structural Characterization and NOR Electroactivity of PdS₂

The geometric structure of pentagonal PdS₂ is composed of three-atom-thick layers arranged in an S–Pd–S configuration, where a Pd layer is encapsulated between two S layers to form a sandwiched-like structure [28], and its monolayer structure and bulk are as illustrated in Fig. 1a, b, respectively. The synthesized PdS₂ exhibits good crystallinity, as confirmed by their X-ray diffraction (XRD) pattern (Fig. 1c) showing several strong diffraction peaks that correspond well to the JCPDS No.72–1198. By scanning electron microscopy (SEM) and transmission electron microscopy (TEM), it can be clearly observed that the synthesized PdS₂ has a quadrilateral nanoplate structure in Fig. 1d, e, whose thickness is about 75 nm. A lattice spacing of 0.217 nm measured in the high-resolution TEM (HRTEM) image (Fig. 1f) is well matched to the (202) lattice plane of orthorhombic PdS₂, which is consistent with result of the lattice fringe measurement by the simulated fast Fourier transform (FFT) and the corresponding FFT pattern reveals that the orthorhombic PdS₂ was monocrystalline. Especially, the characteristic diffraction spot pattern (Fig. 1g) obtained from selected area electron diffraction (SAED) aligns with orthorhombic PdS₂ (JCPDS No. 72–1198), as well as the corresponding simulated diffraction pattern (Fig. 1g, inset), conclusively confirming the monocrystalline nature of the synthesized PdS₂ nanoplates. Figure 1h displays the electrocatalytic NOR performance of PdS₂ nanoplates at different potentials obtained by chronoamperometry (CA) test, with the NO₃[−] yield and FE as indicators, which are determined

by an IC and calculated by a standard curve of NO₃[−] in Fig. S1. It is found that 2.15 V (vs. RHE) is the optimum potential of NOR electrocatalyzed by PdS₂ nanoplates, with the highest NO₃[−] yield of 15.94 μg h^{−1} mg^{−1}_{act.} and the maximum FE of 7.31%. Obviously, the generated nitrate is exclusively derived from N₂, because that no nitrate can be detected in the electrolyte after electrocatalyzed by CC under N₂ atmosphere or by PdS₂ under Ar atmosphere at 2.15 V, even under N₂ atmosphere without external voltage in Fig. 1i. However, the practical application of PdS₂ nanoplates for nitrate electrosynthesis is still hindered by the poor cycling performance (Fig. 1j).

3.2 Improved NOR Electroactivity of PdS₂ with Unique Imitating Growth Feature by Interface Engineering

As reported, the electrocatalytic activity and stability can be effectively enhanced by interface engineering [32], which is attributed to the distinct phase properties at the interface, directly impacting the adsorption energy and electron transport kinetics of intermediate products on either side of the electrocatalytic reaction interface [33]. Building 2D/2D heterostructures is a popular approach for interface engineering, which can availably improve the nitrogen fixation performance of electrocatalysts [21, 34]. Through adjusting the contents of Pd precursor, sulfur source and substrate, PdS₂ nanoplates can be anchored on the surface of the pre-prepared GO, PPy/GO and PVEIB/PPy/GO for constructing typical 2D/2D heterostructures to improve the NOR electroactivity, as illustrated in Fig. 2a. The morphologies of the three substrates are displayed in Fig. S3. The linear sweep voltammetry (LSV) curves of all the electrocatalysts based on PdS₂ in Fig. S4 present that the current density (*j*) obtained in N₂-saturated electrolyte is higher than that obtained in Ar-saturated electrolyte, indicating the occurrence of NOR process catalyzed by these electrocatalysts. Obviously in Fig. 2c, d, the NO₃[−] yield detected by ion chromatography and the corresponding FE can be significantly promoted due to the electrocatalysis of PdS₂@GO, PdS₂@PPy/GO and PdS₂@PVEIB/PPy/GO in the potential range of 1.65–2.35 V (vs. RHE), generated by electrocatalytic NOR in an H-type cell (Fig. 2b) and the corresponding chronoamperometry curves are shown in Fig. S5. Table S1 lists the Pd content determined by an inductively coupled plasma-optical emission spectrometry (ICP-OES) and the corresponding calculated

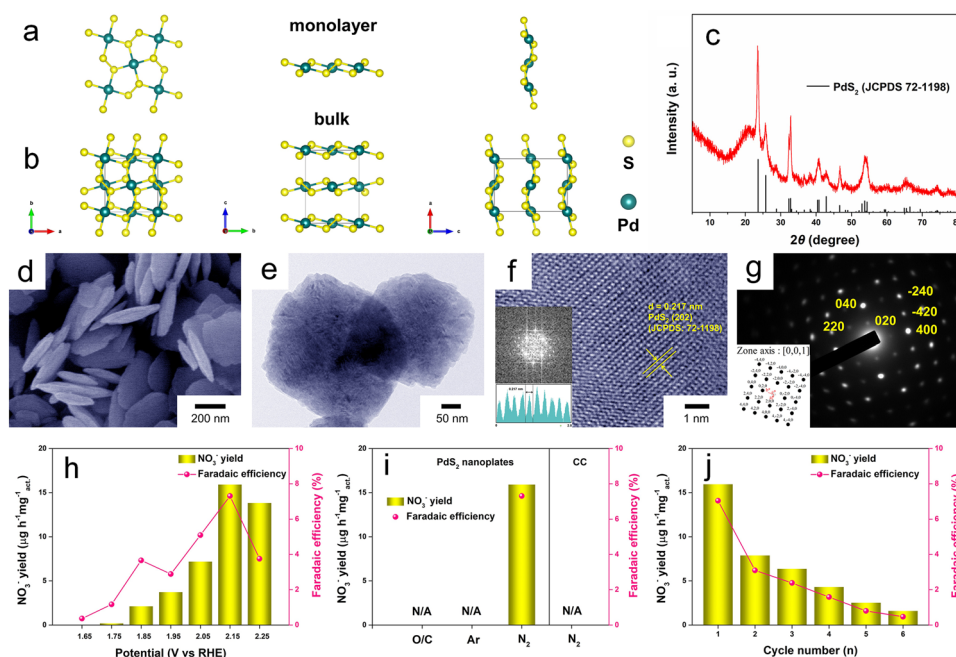


Fig. 1 Top and side views of the pentagonal PdS₂ **a** monolayer and **b** bulk; **c** XRD pattern, **d** SEM, **e** TEM, **f** HRTEM image with FFT pattern and **g** SAED pattern with the corresponding simulated diffraction pattern of PdS₂ nanoplates; **h** NO₃⁻ yield and FE of PdS₂ nanoplates for NOR at different potentials (vs. RHE); **i** electroactivity of CC (substrate) and PdS₂ nanoplates toward NOR at 2.15 V under different conditions; **j** cyclic test for PdS₂ nanoplates performed six times at 2.15 V under electrolysis for 2 h

PdS₂ loading content of the three electrocatalysts. The optimum potential for electrocatalytic NOR obtained by the pure PdS₂ nanoplates and PdS₂@GO is 2.15 V (vs. RHE), but for PdS₂@PPy/GO and PdS₂@PVEIB/PPy/GO is 2.05 V (vs. RHE), indicating that the existence of PPy with good conductivity is conducive to the electron transport during the NOR process, resulting in reducing the NOR overpotential of the composite catalysts. The highest NO₃⁻ yield reaches to 93.91 μg h⁻¹ mg⁻¹_{act.} obtained by PdS₂@PVEIB/PPy/GO at 2.05 V, with the corresponding FE of 7.36%. Though PdS₂@GO presents the highest FE at each potential among the three catalysts (Fig. 2d), with the maximum NO₃⁻ yield of 93.39 μg h⁻¹ mg⁻¹_{act.} at 2.15 V (Fig. 2c) comparable to that of PdS₂@PVEIB/PPy/GO, the cycle stability of PdS₂@GO for NOR is very poor, which is similar to the pure PdS₂ nanoplates. The NO₃⁻ yield and FE obtained by PdS₂@GO at 2.15 V rapidly decrease during six cycles, left to 18.4% of the initial value (Fig. 2e), while PdS₂@PPy/GO exhibits the improved NOR stability with only a little decrease of the NO₃⁻ yield and FE obtained at 2.05 V after six cycles (Fig. 2f). Especially, PdS₂@PVEIB/PPy/GO exhibits the excellent NOR stability with only a slight fluctuation of both

NO₃⁻ yield and FE at 2.05 V for six cycles in Fig. 2g. Obviously, the excellent NOR stability obtained by PdS₂@PPy/GO and PdS₂@PVEIB/PPy/GO is attributed to the contribution of PPy with good conductivity, facilitating the electron conduction and avoiding the charge accumulation during the NOR process, which results in the continuous occurrence of NOR on the electrocatalysts. Analysis of the ion chromatograms of standard NO₃⁻ and NO₂⁻ in Fig. 2h reveals the detection of only NO₃⁻ in N₂-saturated electrolyte when electrocatalyzed by PdS₂@GO, PdS₂@PPy/GO and PdS₂@PVEIB/PPy/GO, indicating the perfect selectivity of the 2D/2D heterostructures based on PdS₂ for NOR in the nitrate electrocatalysis. In addition, no nitrate can be detected in the electrolyte after electrocatalyzed by CC under N₂ atmosphere or by PdS₂@PVEIB/PPy/GO under Ar atmosphere at 2.05 V, as well as under N₂ atmosphere without external voltage in Fig. 2i, suggesting that the generated nitrate is exclusively derived from N₂ through the electrocatalytic action of PdS₂@PVEIB/PPy/GO. Compared to the reported NOR electrocatalysts listed in Table S2, Fig. 2j presents the NOR electroactivity of PdS₂@PVEIB/PPy/GO is at the forefront, contributed by the synergistic effect of each component.

For further exploring why PdS₂@PVEIB/PPy/GO exhibits the excellent electrocatalytic NOR performance, the morphologies and structures of PdS₂@GO, PdS₂@PPy/GO and PdS₂@PVEIB/PPy/GO, as well as PdS₂@PVEIB/PPy/GO after long term NOR, are thoroughly characterized by using SEM, HRTEM, XRD and X-ray photoelectron spectroscopy (XPS) method. All of the electrocatalysts as synthesized present typical 2D/2D heterostructures, but interestingly, significant differences are evident in the morphology of PdS₂ when deposited on different substrates, which present a unique feature of imitating growth. As shown in Fig. 1d–g, the pure PdS₂ nanoplates present the quadrilateral shapes with the thickness of about 75 nm, which is monocrystalline by the evidence of the characteristic diffraction spot pattern. For PdS₂@GO, PdS₂ presents a large and thin layer structure similarly to GO, whose thickness is reduced to 12–20 nm (Fig. S6a, b), while four well-defined concentric diffraction rings appear in the SAED pattern of PdS₂@GO corresponding to the (002), (111), (200) and (022) lattice plane (Fig. S6c, inset), respectively, demonstrating that PdS₂ growing on GO is polycrystalline with the arbitrary crystal orientation. The irregularly shaped PdS₂ with the thickness closed to the pure PdS₂ nanoplates can be observed on PPy/GO in Fig. S7a, b, whose SAED pattern displays that four concentric diffraction rings are composed of many diffraction spots (Fig. S7c, inset), indicating that PdS₂ growing on PPy/GO is polycrystalline with the limited crystal orientation.

Particularly, when PVEIB/PPy/GO is selected as the substrate, the well-defined thin and small PdS₂ nanoplates with the thickness of about 25 nm are anchored on curled lamella surfaces (Fig. 3a, b) due to the induction and the confinement effect of PVEIB, which is derived from the steric hindrance constructed by imidazolium groups. Besides two lattice spacings calculated to 0.380 and 0.268 nm corresponding to the (002) and (200) lattice plane observed in the HRTEM images of PdS₂@PVEIB/PPy/GO as synthesized with the amplified images of the region enclosed by two yellow squares of (c₁) and (c₂), many defects also appear in the region enclosed by the yellow squares of (c₃), which may create more exposed active sites and further accelerate the NOR process, thus resulting in the higher NO₃⁻ yield and FE. The two lattice spacings are consistent with results of the lattice fringe measurement by the simulated FFT in Fig. 3c₁ and 3c₂, respectively. The SAED pattern of PdS₂@PVEIB/PPy/GO in Fig. 3d presents a typical diffraction spot pattern, well matching to the (200), (220), (240), (040), (420),

and (440) lattice plane of orthorhombic PdS₂ (JCPDS No. 72–1198), demonstrating that the thin PdS₂ nanoplates in PdS₂@PVEIB/PPy/GO as synthesized are monocrystalline, which are consistent with the corresponding simulated diffraction pattern (Fig. 3d). The variations in crystallinity and lamellar thickness of PdS₂ nanoplates anchored on the different substrates may be caused by the different induction of the exposed chemical groups on the substrates, which influence the growth characteristic for PdS₂. Comparing the XRD patterns of the pure PdS₂ nanoplates, PdS₂@GO, PdS₂@PPy/GO and PdS₂@PVEIB/PPy/GO (Figs. 1c, S6d, S7d, and 3e), a significant difference can be observed in their crystallinity. The thinner the thickness of PdS₂ nanoplates are, the poorer their crystallinity is, resulting in more defects, which will further present better electrocatalytic NOR performance in possible. In addition, the peaks of C, N, O, Pd and S appear in Fig. 3f determined by energy-dispersive X-ray spectrometer (EDS), and the corresponding elemental mapping images in Fig. 3g present that the profiles of Pd and S element are visually differentiated from that of C, N, O element, well demonstrating the excellent inorganic/organic hierarchical 2D/2D heterostructures of PdS₂@PVEIB/PPy/GO.

After electrolysis for 30 h in N₂ saturated electrolyte, the morphology of PdS₂@PVEIB/PPy/GO remains the same, while the thickness of PdS₂ nanoplates has increased a little in Fig. 3a and b, resulting from the layer number of (002) lattice plane significantly increases after NOR, as shown in the HRTEM image (Fig. 3c), especially the amplified image of the region enclosed by the yellow squares of (c₁). Even so, the thin PdS₂ nanoplates in PdS₂@PVEIB/PPy/GO after NOR are still monocrystalline, testified by the typical diffraction spot pattern also appearing in SAED pattern (Fig. 3d). Obviously seen in the XRD patterns of PdS₂@PVEIB/PPy/GO before and after NOR, the intensity of diffraction peaks in Fig. 3e is much stronger than that in Fig. 3e, derived from the increase of the thickness of PdS₂ nanoplates after NOR, resulting in the improved crystallinity of PdS₂. In addition, after NOR, two additional peaks of F and K appear in Fig. 3f with the corresponding elemental mapping images in Fig. 3g, caused by the added Nafion perfluorinated resin and the adsorbed KOH. Therefore, PdS₂@PVEIB/PPy/GO demonstrates outstanding stability in terms of morphology, crystal structure and chemical components during the NOR process, which may be one of the reasons for its exceptional stability in NOR electrocatalysis.

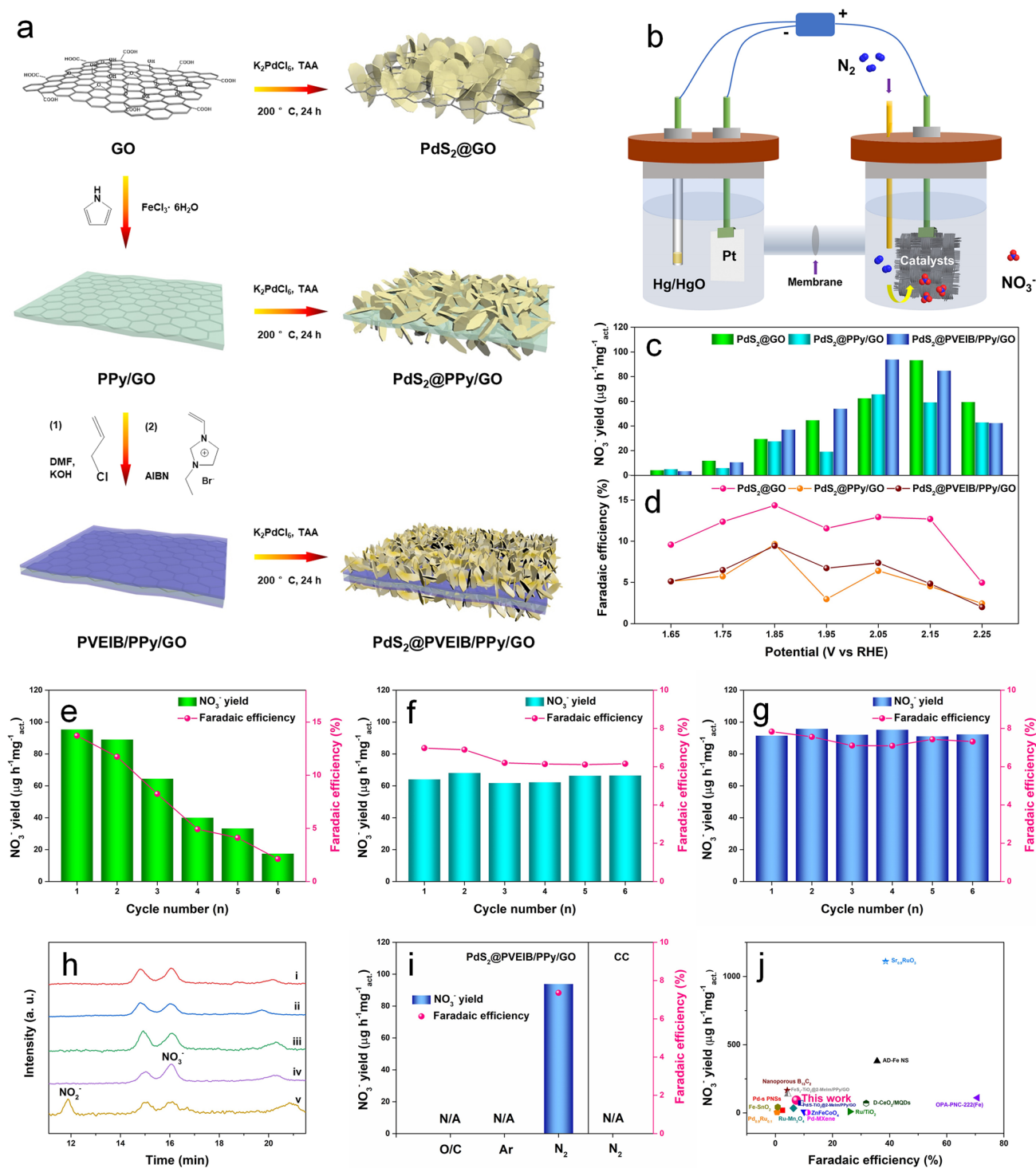


Fig. 2 **a** Schematic of the synthetic process of $PdS_2@GO$, $PdS_2@PPy/GO$ and $PdS_2@PVEIB/PPy/GO$; **b** Schematic of an H-type cell for NOR; **c** NO_3^- yield and **d** FE of $PdS_2@GO$, $PdS_2@PPy/GO$ and $PdS_2@PVEIB/PPy/GO$ for NOR at different potentials (vs. RHE); cyclic test for **e** $PdS_2@GO$ at 2.15 V, **f** $PdS_2@PPy/GO$ and **g** $PdS_2@PVEIB/PPy/GO$ at 2.05 V under electrolysis for 2 h performed six times; **h** Ion chromatograms of the diluted electrolyte after NOR by i) $PdS_2@GO$, ii) $PdS_2@PPy/GO$ and iii) $PdS_2@PVEIB/PPy/GO$ at 2.05 V, iv) the standard NO_3^- of $0.2 \mu g mL^{-1}$, v) the standard NO_2^- of $0.2 \mu g mL^{-1}$; **i** Electroactivity of CC (substrate) and $PdS_2@PVEIB/PPy/GO$ toward NOR at 2.05 V under different conditions; **j** Comparison of NOR electrocatalytic performance with some reported catalysts (see detailed information in Table S2)

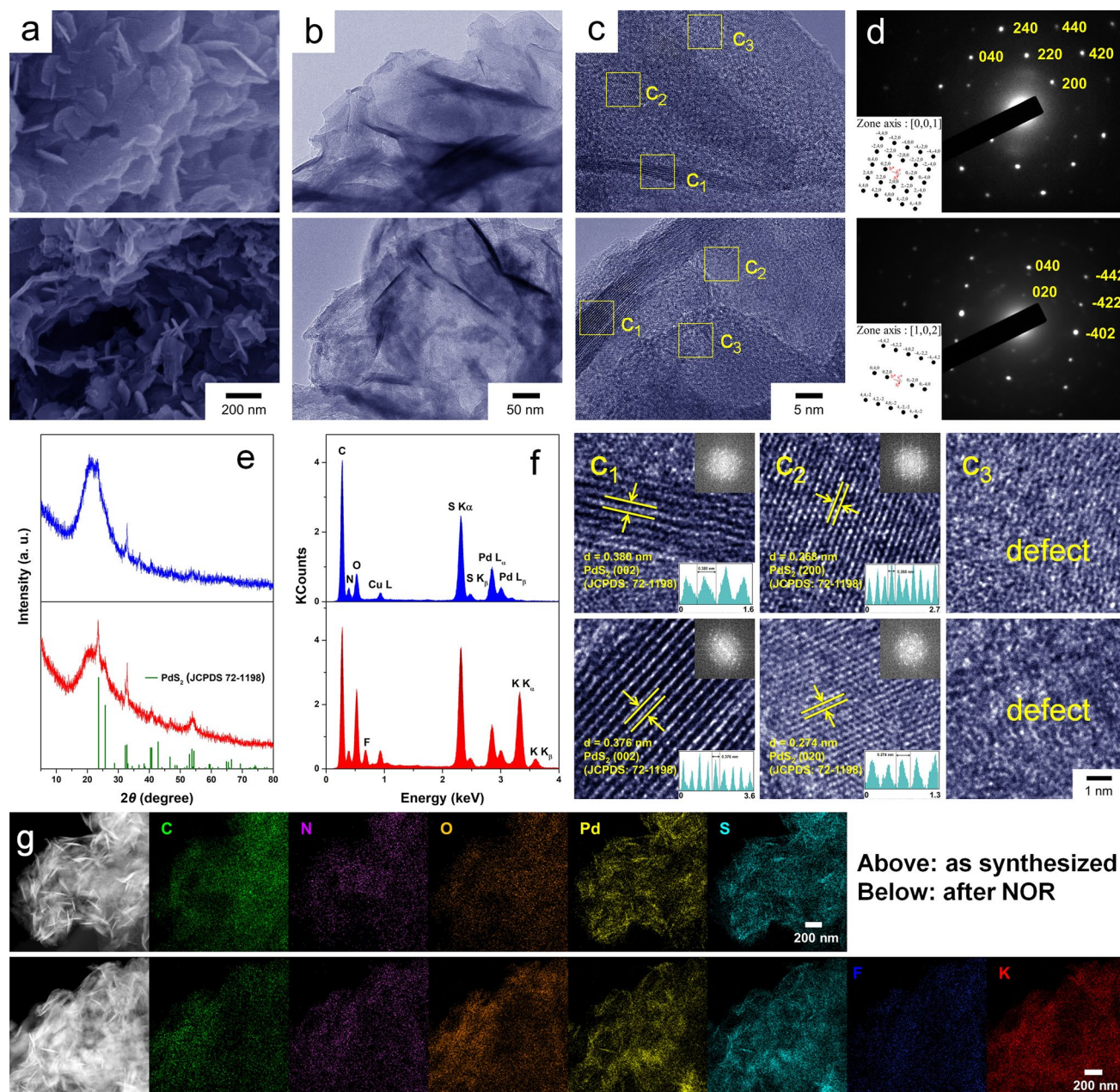


Fig. 3 **a** SEM, **b** TEM, **c** HRTEM images (with the amplified images of the region enclosed by three yellow squares of (c₁), (c₂), (c₃) and the corresponding FFT pattern), **d** SAED pattern with the corresponding simulated diffraction pattern, **e** XRD patterns, **f** EDS spectra and **g** high-angle annular dark field (HAADF) images of PdS₂@PVEIB/PPy/GO (above: as synthesized, below: after electrolysis for 30 h in N₂ saturated electrolyte) with the corresponding elemental mapping of C, N, O, Pd, S, F, K

3.3 Investigation of NOR Mechanism Based on PdS₂

In order to explore the NOR mechanism, the catalytic centers of PdS₂@PVEIB/PPy/GO must be firstly ascertained. It is apparent that all the substrates, including GO, PPy/GO and PVEIB/PPy/GO, have almost no NOR electroactivity

at 2.05 V (Fig. 4a), definitely demonstrating that PdS₂ is real catalytic center for NOR in the all composite catalysts. Obviously, all the constructed 2D/2D heterostructures based on PdS₂, including PdS₂@GO, PdS₂@PPy/GO and PdS₂@PVEIB/PPy/GO, have exhibited the significantly improving NOR electroactivity compared to the pure PdS₂ nanoplates.

The double-layer capacitance (C_{dl}) of the pure PdS₂ nanoplates, PdS₂@GO, PdS₂@PPy/GO and PdS₂@PVEIB/PPy/GO obtained from the cyclic voltammetry (CV) plots in Fig. S8 are calculated to 0.066, 0.132, 0.460 and 1.81 mF cm⁻² in Fig. 4b. Thus, the electrochemical active surface area (ECSA) of all the electrocatalysts based on PdS₂ can be estimated to 1.5, 3.3, 11.5 and 42.45 cm²/cm² from their C_{dl} by Eq. S3, indicating PdS₂@PVEIB/PPy/GO possesses the largest ECSA among them. Figure 4c presents the Nyquist diagrams of the above four electrocatalysts modified glassy carbon electrode (GCE) obtained by the electrochemical impedance spectroscopy (EIS). They all display only “one semicircle” feature at the potential of 2.05 V (vs. RHE), and the smallest semicircle domain is obviously found in the Nyquist plot of PdS₂@PVEIB/PPy/GO in Fig. 4c-iv, implying that the charge-transfer resistance (R_{ct}) can be significantly reduced by the synergistic effect of each component in PdS₂@PVEIB/PPy/GO. It is demonstrated that a higher charge-transfer rate can be achieved by PdS₂@PVEIB/PPy/GO, accelerating the NOR process and resulting in the better NOR electroactivity.

According to the above results, PdS₂ nanoplates were selected for electrochemical in situ ATR-SEIRAS test to detect the reaction intermediates of NOR, availing to eliminate other interference and elucidate the mechanistic pathway underlying the electrocatalysis of N₂ conversion to NO₃⁻ by PdS₂ nanoplates in alkaline conditions. The spectra of real-time ATR-SEIRAS are captured during the anodic scan of PdS₂ nanoplates in a N₂-saturated 0.1 M KOH solution from 1.55 to 2.25 V (vs. RHE) (Fig. 4b). Obviously, the intensity of two prominent absorption bands at 1245 and 1646 cm⁻¹ corresponding to bridging nitrate exhibits a progressive increase as the potential range extends from 1.6 to 2.25 V (vs. RHE), along with the monodentate nitrate at 1635 cm⁻¹ [35]. Three distinct bands associated with adsorbed N-containing oxide species are observed at approximately 1320, 1420, and 1466 cm⁻¹, corresponding to bridging bidentate nitrites [36], NO₃⁻ vibration [37] and the N=O stretching vibration of linear nitrites [35], respectively. Figure 4c presents the potential dependence of the bridging nitrate vibration at 1245 and 1646 cm⁻¹ and the corresponding LSV curve (black shot dot line) under N₂ atmosphere. Two bands exhibit a significant increase in intensity as the potential range from 1.6 to 2.25 V (vs. RHE), concurrent with the rise in oxidation current, suggesting an increased coverage of adsorbed *NO₃⁻ on PdS₂ nanoplates.

Based on the observed intermediates, the associative distal pathway for NOR is inferred through DFT calculations performed on a PdS₂ (002) monolayer with an S-vacancy, whose structure is displayed in Fig. 4d and constructed from HRTEM measurements in Fig. 3. The calculated Gibbs free energy (ΔG) diagram of the NOR kinetic pathway on the S-vacancy of PdS₂ (002) is displayed in Fig. 4e, with the atomistic structures describing the reaction pathway illustrated in Fig. S9. The step for the oxidation of *N₂ to form *NNOH has the highest energy barrier of 2.95 eV, which is regarded as the potential-determining step (PDS) of the whole NOR process.

3.4 Facilitated NOR Electroactivity of PdS₂ by In Situ Generated Sulfate

Previous theoretical calculations have indicated that monolayer PdS₂ behaves as a typical semiconductor, while bilayer PdS₂ can exhibit the semimetallic property [38]. It is inferred that the transition of PdS₂ from a semiconductor to a semimetal will occur with an increase in the number of layers [39]; in other words, the thicker the PdS₂ nanoplates are, the enhancer the semimetallic property they have. Therefore, this unique imitating growth feature not only has an effect on the thickness and shape of PdS₂, but also significantly affects its electronic state, which can be confirmed by XPS, and finally resulting in the differences to its NOR performance. The Pd 3d and S 2p XPS spectra of the pure PdS₂ nanoplates, PdS₂@GO, PdS₂@PPy/GO and PdS₂@PVEIB/PPy/GO are displayed in Fig. 5a, b. Because the PdS₂ nanoplates with thinner thickness and more defects anchored on GO and PVEIB/PPy/GO are easy to be oxidized, the higher bonding energy of Pd 3d_{5/2} and Pd 3d_{3/2} orbitals of Pd-S bonding appears at 336.9 and 342.1 eV [40] (Fig. 5a-ii and iv), respectively, while the pure PdS₂ nanoplates and PdS₂ nanoplates anchored on PPy/GO present the enhanced semimetallic property due to the increased thickness, resulting in the lower bonding energy of Pd 3d_{5/2} and Pd 3d_{3/2} orbitals of Pd-S bonding in Fig. 5a-i and iii.

Due to the unique imitating growth feature, the oxidation degree of PdS₂ nanoplates is affected by thickness and defects during the preparation process or exposed in air, and these differences are visible in S 2p spectra in Fig. 5b. The peak at 168.6 eV corresponding to SO₄²⁻ [41] can be detected in the S 2p spectra of PdS₂@GO and PdS₂@

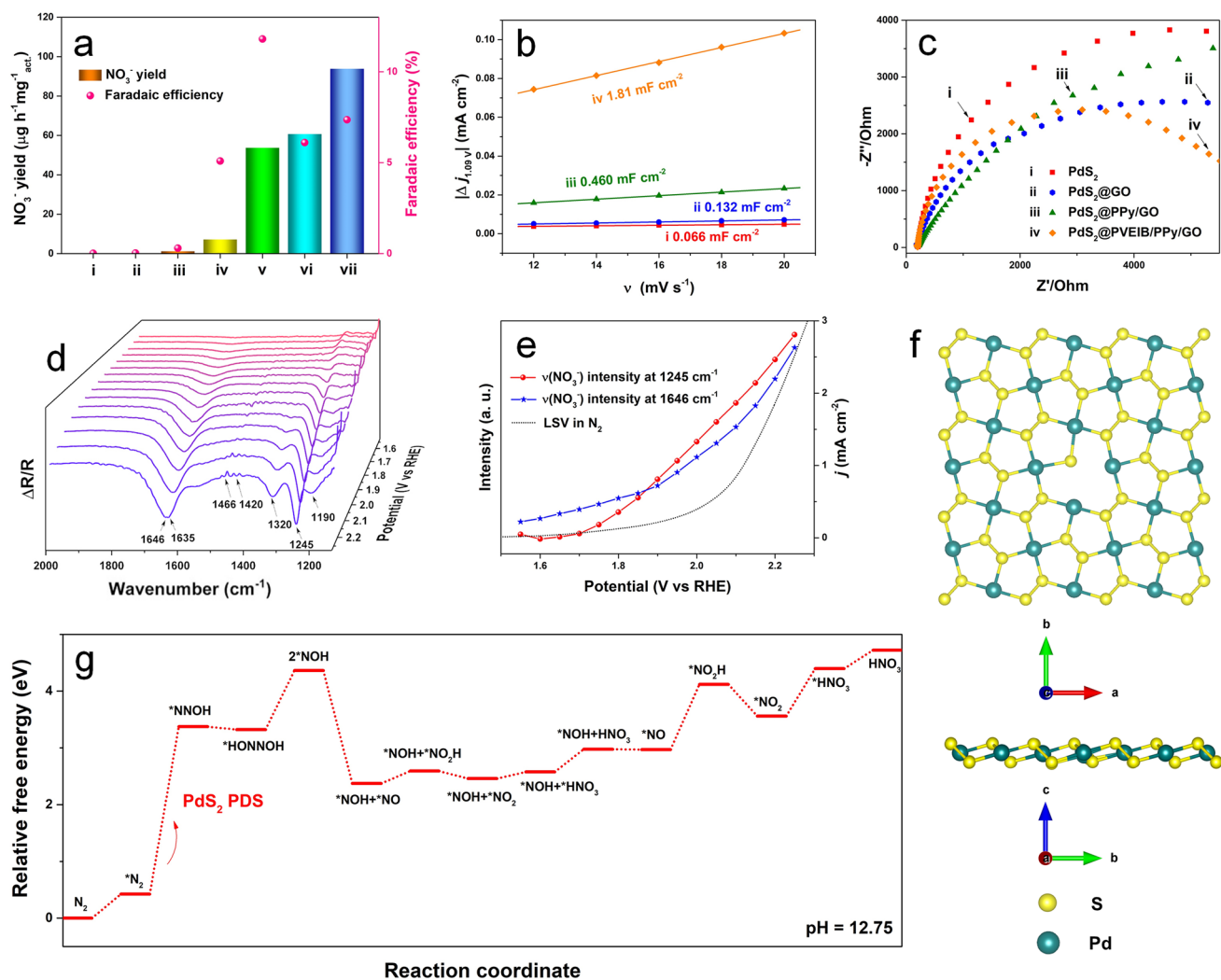


Fig. 4 **a** NO_3^- yield and FE obtained by different electrocatalysts at 2.05 V (vs. RHE) under electrolysis for 2 h: (i) GO, (ii) PPy/GO, (iii) PVEIB/PPy/GO, (iv) PdS_2 , (v) $\text{PdS}_2@\text{GO}$, (vi) $\text{PdS}_2@\text{PPy}/\text{GO}$ and (vii) $\text{PdS}_2@\text{PVEIB}/\text{PPy}/\text{GO}$; **b** C_{dl} of (i) PdS_2 , (ii) $\text{PdS}_2@\text{GO}$, (iii) $\text{PdS}_2@\text{PPy}/\text{GO}$ and (iv) $\text{PdS}_2@\text{PVEIB}/\text{PPy}/\text{GO}$ modified GCE; **c** Nyquist diagrams of (i) PdS_2 , (ii) $\text{PdS}_2@\text{GO}$, (iii) $\text{PdS}_2@\text{PPy}/\text{GO}$ and (iv) $\text{PdS}_2@\text{PVEIB}/\text{PPy}/\text{GO}$ modified GCE in 1 M KOH recorded at DC potential of 2.05 V (vs. RHE); **d** Electrochemical in situ ATR-SEIRAS of PdS_2 nanoplates from 1.55 to 2.25 V (vs. RHE) in N_2 -saturated 0.1 M KOH electrolyte; **e** Potential-dependent peak intensity of NO_3^- vibration (1245 and 1646 cm^{-1}) derived from **d** and the corresponding LSV curve in N_2 -saturated 0.1 M KOH electrolyte; **f** Top view of the (002) surface of PdS_2 monolayer with an S-vacancy; **g** Relative free energy diagram for NOR under alkaline conditions over the (002) surface of PdS_2 monolayer with sulfur vacancy

PVEIB/PPy/GO (Fig. 5b-ii and iv), caused by the in situ oxidation of the defects on the thinner PdS_2 nanoplates during the preparation process or exposed in air. Especially, $\text{PdS}_2@\text{GO}$ presents the obviously stronger peak of SO_4^{2-} , compared to $\text{PdS}_2@\text{PVEIB}/\text{PPy}/\text{GO}$, indicating the higher oxidation degree of PdS_2 nanoplates on GO, which may be caused by the thinner the PdS_2 nanoplates are, the more defects they have, and the easier they are to be oxidized. No peak related to SO_4^{2-} can be fitted in the S 2p spectra

of the pure PdS_2 nanoplates and $\text{PdS}_2@\text{PPy}/\text{GO}$ (Fig. 5b-i and iii), due to the enhanced thickness of PdS_2 nanoplates with better crystallinity and less defects. The above difference of the oxidation degree of PdS_2 nanoplates anchored on different substrates can be also verified by their Pd L_{3-} edge high energy resolution fluorescence detected X-ray absorption near-edge (HERFD-XANES) spectra (Fig. 5c). It can be clearly observed that the position of the main, intense white line shifts to higher energy from Pd foil to PdS_2 , while

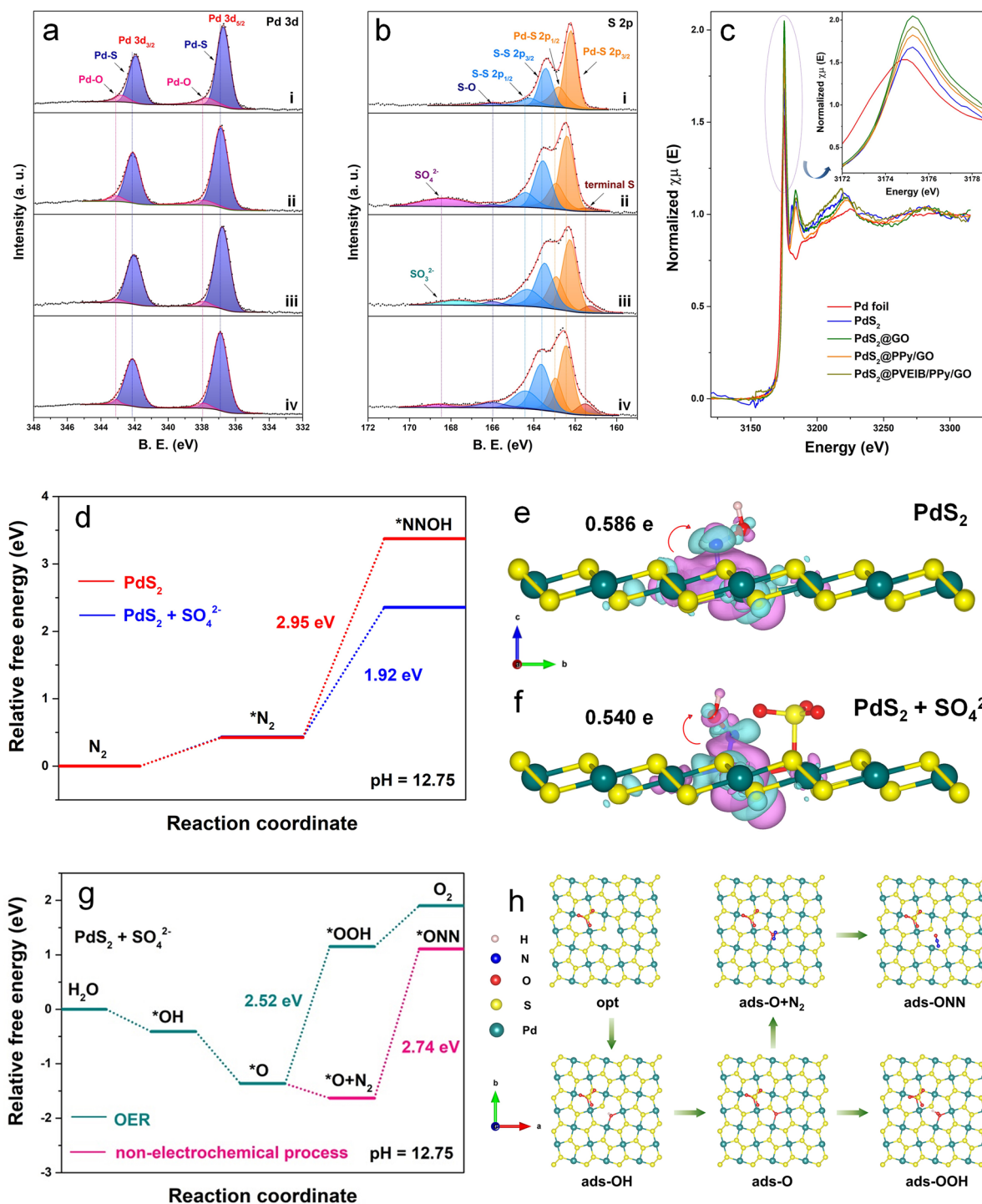


Fig. 5 **a** Pd 3d and **b** S 2p spectra by XPS of (i) PdS₂ nanoplates, (ii) PdS₂@GO, (iii) PdS₂@PPy/GO and (iv) PdS₂@PVEIB/PPy/GO; **c** Normalized Pd L₃-edge HERFD-XANES spectra for various electrocatalysts based on PdS₂; **d** Relative free energy diagram of N₂ electrooxidation process on PdS₂ and PdS₂+SO₄²⁻; charge density difference of *NNOH adsorbed on **e** PdS₂ and **f** PdS₂+SO₄²⁻, where the isosurface value is set to be 0.002 e Å⁻³ and the magenta and cyan isosurfaces stand for the electron depletion and accumulation, respectively; **g** Relative free energy diagram OER process and **h** the corresponding atomistic structure scheme for describing the reaction pathway of OER on PdS₂+SO₄²⁻, as well as the non-electrochemical process of NOR

the white line intensity follows the order of $\text{PdS}_2 < \text{PdS}_2/\text{PPy}/\text{GO} < \text{PdS}_2@\text{PVEIB}/\text{PPy}/\text{GO} < \text{PdS}_2@\text{GO}$, further demonstrating that the oxidation degree of PdS_2 nanoplates anchored on GO and PVEIB/PPy/GO is higher than that anchored on PPy/GO, and the lowest is the pure PdS_2 nanoplates.

Based on the above results and the differences in the NO_3^- yield and FE obtained by the four electrocatalysts in Figs. 1h and 2c, it can be inferred that the existence of in situ generated SO_4^{2-} would remarkably promote the NOR electroactivity of PdS_2 . In order to further verify this conjecture, a $\text{PdS}_2 + \text{SO}_4^{2-}$ structure model has been optimized by the in situ generated SO_4^{2-} on a (002) surface of PdS_2 monolayer with an S-vacancy, as shown in Fig. S10. The calculated Gibbs free energy (ΔG) diagram of N_2 electrooxidation process on PdS_2 and $\text{PdS}_2 + \text{SO}_4^{2-}$ is presented in Fig. 5d. Obviously, the energy barrier for the oxidation of $^*\text{N}_2$ to form $^*\text{NNOH}$ on $\text{PdS}_2 + \text{SO}_4^{2-}$ reduces to 1.92 eV by DFT calculations, indicating that the in situ generated SO_4^{2-} can effectively reduce the activation energy of the PDS, thus accelerating NOR [16]. Subsequently, the charge density difference of NNOH adsorbed on PdS_2 and $\text{PdS}_2 + \text{SO}_4^{2-}$ is examined to gain a deeper insight into the factors, contributing to the improved NOR activity of the catalysts. As shown in Fig. 5e and f, the NNOH adsorbed on the Pd site of $\text{PdS}_2 + \text{SO}_4^{2-}$ (0.540 e) demonstrates less charge exchange and transfer between NNOH and the Pd atoms than that of NNOH adsorbed on the Pd site of PdS_2 (0.586 e), indicating that the presence of in situ generated SO_4^{2-} can change the amount of electron transfer from the surface to the reaction intermediate, thus reducing the energy barrier and accelerating NOR.

As is well known, electrocatalytic NOR involves activation and cleavage of $\text{N}\equiv\text{N}$ with high bonding energy (941 kJ mol^{-1}) [42], which is very difficult to perform kinetically and inevitably hindered by the competition from OER in aqueous solutions containing electrolytes [43]. For $\text{PdS}_2@\text{PVEIB}/\text{PPy}/\text{GO}$, the existence of SO_4^{2-} can effectively reduce the energy barrier of the PDS (the oxidation of $^*\text{N}_2$ to form $^*\text{NNOH}$) at the defects of PdS_2 (Fig. 4c), but OER is also likely to occur at this active site, calculated by DFT in Fig. 5g. Though the appropriate amount of sulfate ions (originated from chemical modification in the preparation process of the electrocatalysts or physical absorption from the electrolyte containing SO_4^{2-}) existing on the surface of electrocatalysts, can be

also beneficial to stabilize the intermediate of $^*\text{OOH}$, and thus improve the OER performances [44, 45], the PDS of OER at $\text{PdS}_2 + \text{SO}_4^{2-}$ is the step for the combination of $^*\text{O}$ and OH^- to form $^*\text{OOH}$ with the energy barrier of 2.52 eV, which is higher than the PDS of NOR on the same active site (1.92 eV), indicating that this active site is more prone to NOR. In addition, as claimed in previous works, the non-electrochemical step of NOR is closely related to the presence of weakly adsorbed oxygen species ($^*\text{O}$) generated from the competitive OER on the surface of electrocatalysts [46]. $^*\text{O}$ can react with N_2 in a non-electrochemical process ($^*\text{O} + \text{N}_2 \rightarrow ^*\text{ONN}$) [47]. For the constructed $\text{PdS}_2 + \text{SO}_4^{2-}$, the energy barrier for the formation of $^*\text{ONN}$ is calculated to 2.74 eV, which is higher than the PDS of OER (2.52 eV) at this active site, suggesting that the occurrence of NOR is dominated by the electrochemical oxidation process of N_2 . The corresponding atomistic structure scheme for describing the reaction pathway of OER on $\text{PdS}_2 + \text{SO}_4^{2-}$ is presented in Fig. 5h, as well as the non-electrochemical process of NOR.

XPS analysis can provide additional confirmation of the chemical states of $\text{PdS}_2@\text{PVEIB}/\text{PPy}/\text{GO}$ before and after electrolysis for 30 h in N_2 saturated electrolyte. For $\text{PdS}_2@\text{PVEIB}/\text{PPy}/\text{GO}$ as synthesized, C 1s, N 1s, O 1s, Pd 3d, S 2s, and S 2p peaks are detected in its survey spectrum (Fig. 6a-i). The fitted C 1s, N 1s, and O 1s peaks in Fig. 6b-i, 6c-i and 6d-i can well verify the existence of GO, PPy and PVEIB, listed in Table S3 in detail. Especially, a peak fitted at 401.5 eV ascribed to N^+ in the imidazolium ring appeared in the N 1s XPS spectra in Fig. 6c-i, which can well testify that PVEIB has been linked on the surface of PPy/GO. The F 1s peak and two peaks at 291.8, 293.5 eV belonging to CF_2 , CF_3 groups [48, 49] are detected in the survey and C 1s spectra of $\text{PdS}_2@\text{PVEIB}/\text{PPy}/\text{GO}$ after NOR (Figs. 6a-ii and b-ii), respectively, caused by the added Nafion perfluorinated resin, while two peaks attributed to $\text{K}^+ 2p_{3/2}$ (292.6 eV) [50] and $\text{K}^+ 2p_{1/2}$ (295.7 eV) [51], as well as an additional peak related to OH^- (530.7 eV) [52] appear in C 1s and O 1s spectra of $\text{PdS}_2@\text{PVEIB}/\text{PPy}/\text{GO}$ after NOR (Fig. 6b-ii and Fig. 6d-ii), respectively, resulting from the adsorbed KOH. It is noteworthy that both peaks associated to the Pd $3d_{5/2}$ and Pd $3d_{3/2}$ orbitals of Pd-S bonding exhibit a negative shift of approximately 0.1 eV in the Pd 3d spectrum of $\text{PdS}_2@\text{PVEIB}/\text{PPy}/\text{GO}$ after NOR (Fig. 6e-ii). It may be caused by the increase in the number of PdS_2 layers, which

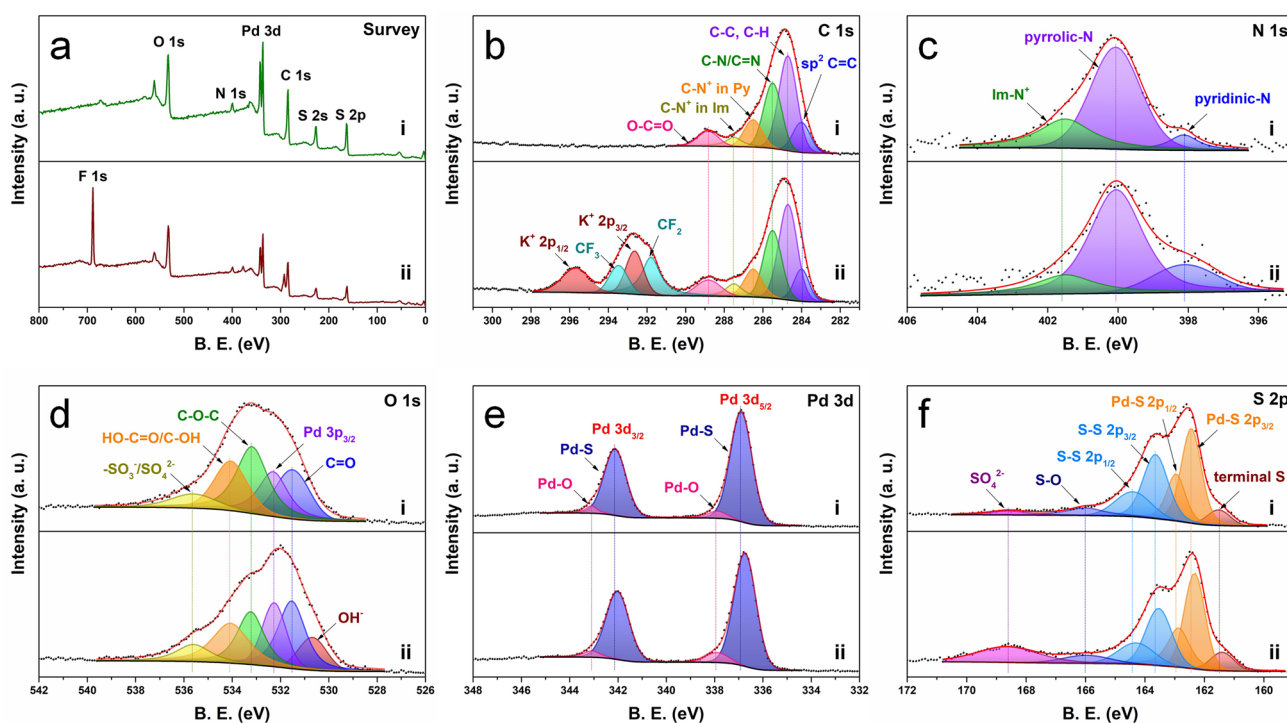


Fig. 6 XPS spectra of PdS₂@PVEIB/PPy/GO (i) before and (ii) after electrolysis for 30 h in N₂ saturated electrolyte: **a** survey, **b** C 1s, **c** N 1s, **d** O 1s, **e** Pd 3d and **f** S 2p

leads to the enhanced semimetallic property of PdS₂, thus allowing the electrocatalyst to sustain a high NOR electroactivity. In the S 2p region of PdS₂@PVEIB/PPy/GO as synthesized (Fig. 6f-i), the peaks corresponding to terminal S (161.5 eV) [53], Pd-S (162.4, 163.0 eV) [54] and bridging S (163.6, 164.4 eV) [55, 56] are well consistent with the bonding modes of the S element in PdS₂, respectively, which also negatively shift by about 0.1 eV in Fig. 6f-ii, similarly suggesting the enhanced semimetallic property of PdS₂. In addition, the peak intensity of SO₄²⁻ located at 168.6 eV [41] is significantly enhanced in Fig. 6f-ii, derived from the in situ oxidation of S in PdS₂ at the high NOR potential, which can help to remain the lower activation energy of the PDS and extend the high NOR electroactivity of PdS₂, ultimately resulting in the excellent NOR stability of PdS₂@PVEIB/PPy/GO.

4 Conclusions

In summary, the catalytic activity and stability of PdS₂ nanoplates toward NOR were significantly enhanced when anchored on different substrates to form 2D/2D

heterostructures due to its unique imitating growth feature. The obtained PdS₂@PVEIB/PPy/GO exhibited the excellent NOR electroactivity with the highest NO₃⁻ yield of 93.91 μg h⁻¹ mg⁻¹_{act.} and the maximum FE of 7.36% at 2.05 V (vs. RHE), as well as the outstanding stability and selectivity. The improved NOR performance could be contributed by the synergistic effect of each component, including PPy for facilitating electron transport, GO for providing large surface area, PVEIB for inducing defects in PdS₂ nanoplates and the thin PdS₂ nanoplates with the excellent activation capacity to N₂ for acting as catalytic centers. The in situ generation of SO₄²⁻ caused by the oxidation of thin and small PdS₂ nanoplates with defects during the preparation process or exposed in air, as well as at high NOR potential, was found to reduce the activation energy of the reaction, accelerating NOR. This research would provide valuable insights for the development of novel electrocatalysts based on NTMDs for the applications in the electrosynthesis of nitrate.

Acknowledgements T. M. acknowledged the Australian Research Council (ARC) through Future Fellowship (FT210100298), Discovery Project (DP220100603), Linkage Project (LP210200504,

LP220100088, LP230200897) and Industrial Transformation Research Hub (IH240100009) schemes, the Australian Government through the Cooperative Research Centres Projects (CRCPX-III000077), the Australian Renewable Energy Agency (ARENA) as part of ARENA's Transformative Research Accelerating Commercialisation Program (TM021) and European Commission's Australia-Spain Network for Innovation and Research Excellence (AuSpire). R. Z. thanked the Foundation of Liaoning Province Education Administration (2020LQN03) and the Foundation of Liaoning Province Education Administration in 2024 (Independent topic selection-Natural science category-Strategic industrialization project LJ212410163023). S. W. thanked the Scientific Research Fund of Liaoning Provincial Education Department (JYTMS20230767). H. M. thanked the Liaoning Revitalization Talents Program (XLYC2007132). The authors would like to thank Yao Fan and Gao Jilong from Shiyanjia Lab (www.shiyanjia.com) for the TEM, XPS and ICP analysis.

Author Contributions R.Z. revised the article, conducted data analysis and provided financial support for characterization tests and the DFT calculations. H.M. conceived the idea, designed the study, conducted catalyst characterizations and the data analysis, and wrote the article. Z.W. prepared the catalysts and conducted electrochemical tests. S.M. conducted electrochemical tests. S.W. conducted ion chromatography tests. Q.W. and D.L. did the electron microscopy characterizations. H.L. conducted the data analysis. Y.F. conducted the synchrotron radiation characterizations. X.L. polished the article. T.M. revised the article and provided financial support for characterization tests.

Declarations

Conflict of interest The authors declare no interest conflict. They have no known competing financial interests or personal relationships that could have appeared to influence the work reported in this paper.

Open Access This article is licensed under a Creative Commons Attribution 4.0 International License, which permits use, sharing, adaptation, distribution and reproduction in any medium or format, as long as you give appropriate credit to the original author(s) and the source, provide a link to the Creative Commons licence, and indicate if changes were made. The images or other third party material in this article are included in the article's Creative Commons licence, unless indicated otherwise in a credit line to the material. If material is not included in the article's Creative Commons licence and your intended use is not permitted by statutory regulation or exceeds the permitted use, you will need to obtain permission directly from the copyright holder. To view a copy of this licence, visit <http://creativecommons.org/licenses/by/4.0/>.

Supplementary Information The online version contains supplementary material available at <https://doi.org/10.1007/s40820-025-01803-3>.

References

1. L. Ouyang, J. Liang, Y. Luo, D. Zheng, S. Sun et al., Recent advances in electrocatalytic ammonia synthesis. *Chin. J. Catal.* **50**, 6–44 (2023). [https://doi.org/10.1016/S1872-2067\(23\)64464-X](https://doi.org/10.1016/S1872-2067(23)64464-X)
2. I. Shaheen, I. Hussain, T. Zahra, M.S. Javed, S.S. Ahmad Shah et al., Recent advancements in metal oxides for energy storage materials: design classification and electrodes configuration of supercapacitor. *J Energy Storage* **72**, 108719 (2023). <https://doi.org/10.1016/j.est.2023.108719>
3. J. Ba, H. Dong, M. Odziomek, F. Lai, R. Wang et al., Red carbon mediated formation of Cu₂O clusters dispersed on the oxocarbon framework by Fehling's route and their use for the nitrate electroreduction in acidic conditions. *Adv. Mater.* **36**(25), 2400396 (2024). <https://doi.org/10.1002/adma.20240396>
4. A. Zhang, Y. Liang, H. Zhang, Z. Geng, J. Zeng, Doping regulation in transition metal compounds for electrocatalysis. *Chem. Soc. Rev.* **50**(17), 9817–9844 (2021). <https://doi.org/10.1039/D1CS00330E>
5. M. Jiang, M. Zhu, M. Wang, Y. He, X. Luo et al., Review on electrocatalytic coreduction of carbon dioxide and nitrogenous species for urea synthesis. *ACS Nano* **17**(4), 3209–3224 (2023). <https://doi.org/10.1021/acsnano.2c11046>
6. H. Guo, Y. Zhou, K. Chu, X. Cao, J. Qin et al., Improved ammonia synthesis and energy output from zinc-nitrate batteries by spin-state regulation in perovskite oxides. *J. Am. Chem. Soc.* **147**(4), 3119–3128 (2025). <https://doi.org/10.1021/jacs.4c12240>
7. K. Chu, W. Zong, G. Xue, H. Guo, J. Qin et al., Cation substitution strategy for developing perovskite oxide with rich oxygen vacancy-mediated charge redistribution enables highly efficient nitrate electroreduction to ammonia. *J. Am. Chem. Soc.* **145**(39), 21387–21396 (2023). <https://doi.org/10.1021/jacs.3c06402>
8. T. Li, S. Han, C. Wang, Y. Huang, Y. Wang et al., Ru-doped Pd nanoparticles for nitrogen electrooxidation to nitrate. *ACS Catal.* **11**(22), 14032–14037 (2021). <https://doi.org/10.1021/acscatal.1c04360>
9. Z. Wang, J. Liu, H. Zhao, W. Xu, J. Liu et al., Free radicals promote electrocatalytic nitrogen oxidation. *Chem. Sci.* **14**(7), 1878–1884 (2023). <https://doi.org/10.1039/d2sc06599a>
10. H. Mao, Y. Sun, H. Li, S. Li, D. Liu et al., Electrosynthesis of nitrate by Pd and TiO₂ nanoparticles anchored on 2-methylimidazolium functionalized polypyrrole/graphene oxide. *Electrochim. Acta* **482**, 143978 (2024). <https://doi.org/10.1016/j.electacta.2024.143978>
11. Z. Nie, L. Zhang, X. Ding, M. Cong, F. Xu et al., Catalytic kinetics regulation for enhanced electrochemical nitrogen oxidation by Ru-nanoclusters-coupled Mn₃O₄ catalysts decorated with atomically dispersed Ru atoms. *Adv. Mater.* **34**(14), 2108180 (2022). <https://doi.org/10.1002/adma.202108180>
12. Y. Zhang, F. Du, R. Wang, X. Ling, X. Wang et al., Electrocatalytic fixation of N₂ into NO₃⁻: electron transfer between oxygen vacancies and loaded Au in Nb₂O_{5-x} nanobelts to

- promote ambient nitrogen oxidation. *J. Mater. Chem. A* **9**(32), 17442–17450 (2021). <https://doi.org/10.1039/D1TA03128G>
13. L. Zhang, M. Cong, X. Ding, Y. Jin, F. Xu et al., A Janus Fe-SnO₂ catalyst that enables bifunctional electrochemical nitrogen fixation. *Angew. Chem. Int. Ed.* **59**(27), 10888–10893 (2020). <https://doi.org/10.1002/anie.202003518>
 14. H. Mao, H. Li, Y. Sun, S. Wu, Q. Wu et al., Electrosynthesis of nitrate by FeS₂-TiO₂ heterogeneous nanoparticles supported on 2-methylimidazolium functionalized polypyrrole/graphene oxide. *Chem. Eng. J.* **489**, 151414 (2024). <https://doi.org/10.1016/j.cej.2024.151414>
 15. H. Mao, Y. Sun, H. Li, S. Wu, D. Liu et al., Synergy of Pd²⁺/S²⁻-doped TiO₂ supported on 2-methylimidazolium-functionalized polypyrrole/graphene oxide for enhanced nitrogen electrooxidation. *Adv. Mater.* **36**(16), 2313155 (2024). <https://doi.org/10.1002/adma.202313155>
 16. T. Li, S. Han, C. Cheng, Y. Wang, X. Du et al., Sulfate-enabled nitrate synthesis from nitrogen electrooxidation on a rhodium electrocatalyst. *Angew. Chem. Int. Ed.* **61**(26), e202204541 (2022). <https://doi.org/10.1002/anie.202204541>
 17. G. Chen, C. Zhang, S. Xue, J. Liu, Y. Wang et al., A polarization boosted strategy for the modification of transition metal dichalcogenides as electrocatalysts for water-splitting. *Small* **17**(26), 2100510 (2021). <https://doi.org/10.1002/sml.202100510>
 18. L. Ma, Y. Li, Y. Xu, J. Sun, J. Liu et al., Two-dimensional transition metal dichalcogenides for electrocatalytic nitrogen fixation to ammonia: advances, challenges and perspectives. A mini review. *Electrochem. Commun.* **125**, 107002 (2021). <https://doi.org/10.1016/j.elecom.2021.107002>
 19. M. Wang, L. Zhang, Y. He, H. Zhu, Recent advances in transition-metal-sulfide-based bifunctional electrocatalysts for overall water splitting. *J. Mater. Chem. A* **9**(9), 5320–5363 (2021). <https://doi.org/10.1039/d0ta12152e>
 20. H. Mao, Y. Fu, H. Yang, S. Zhang, J. Liu et al., Structure-activity relationship toward electrocatalytic nitrogen reduction of MoS₂ growing on polypyrrole/graphene oxide affected by pyridinium-type ionic liquids. *Chem. Eng. J.* **425**, 131769 (2021). <https://doi.org/10.1016/j.cej.2021.131769>
 21. H. Mao, Y. Fu, H. Yang, Z.-Z. Deng, Y. Sun et al., Ultrathin 1T-MoS₂ nanoplates induced by quaternary ammonium-type ionic liquids on polypyrrole/graphene oxide nanosheets and its irreversible crystal phase transition during electrocatalytic nitrogen reduction. *ACS Appl. Mater. Interfaces* **12**(22), 25189–25199 (2020). <https://doi.org/10.1021/acsami.0c05204>
 22. H. Mao, H. Yang, J. Liu, S. Zhang, D. Liu et al., Improved nitrogen reduction electroactivity by unique MoS₂-SnS₂ heterogeneous nanoplates supported on poly(zwitterionic liquids) functionalized polypyrrole/graphene oxide. *Chin. J. Catal.* **43**(5), 1341–1350 (2022). [https://doi.org/10.1016/S1872-2067\(21\)63944-X](https://doi.org/10.1016/S1872-2067(21)63944-X)
 23. D. Saraf, S. Chakraborty, A. Kshirsagar, R. Ahuja, In pursuit of bifunctional catalytic activity in PdS₂ pseudo-monolayer through reaction coordinate mapping. *Nano Energy* **49**, 283–289 (2018). <https://doi.org/10.1016/j.nanoen.2018.04.019>
 24. K. He, W. Xu, J. Tang, Y. Lu, C. Yi et al., Centimeter-scale PdS₂ ultrathin films with high mobility and broadband photoresponse. *Small* **19**(17), e2206915 (2023). <https://doi.org/10.1002/sml.202206915>
 25. L. Pi, L. Li, K. Liu, Q. Zhang, H. Li et al., Recent progress on 2D noble-transition-metal dichalcogenides. *Adv. Funct. Mater.* **29**(51), 1904932 (2019). <https://doi.org/10.1002/adfm.201904932>
 26. Y. Ma, X. Gong, F. Xiao, Y. Liu, X. Ming, First-principles study on the selective detection of toxic gases by 2D monolayer PdS₂: insight into charge transfer dynamics and alignment of frontier molecular orbitals. *ACS Appl. Nano Mater.* **6**(13), 12470–12478 (2023). <https://doi.org/10.1021/acsanm.3c02177>
 27. R.O. Figueiredo, L. Seixas, Hydrogen-evolution reaction in two-dimensional PdS₂ by phase and defect engineering. *Phys. Rev. Applied* **17**(3), 034035 (2022). <https://doi.org/10.1103/physrevapplied.17.034035>
 28. J. Li, D. Liang, G. Liu, B. Jia, J. Cao et al., Defect induced electrocatalytic hydrogen properties of pentagonal PdX₂ (X = S, Se). *RSC Adv.* **11**(61), 38478–38485 (2021). <https://doi.org/10.1039/D1RA07466K>
 29. M. Ghorbani-Asl, A. Kuc, P. Miró, T. Heine, A single-material logical junction based on 2D crystal PdS₂. *Adv. Mater.* **28**(5), 853–856 (2016). <https://doi.org/10.1002/adma.201504274>
 30. A. Guha, R. Sharma, K.R. Sahoo, A.B. Puthirath, N. Shyaga et al., One-dimensional hollow structures of 2O-PdS₂ decorated carbon for water electrolysis. *ACS Appl. Energy Mater.* **4**(9), 8715–8720 (2021). <https://doi.org/10.1021/acsam.1c01703>
 31. F. Karimi, M. Akin, R. Bayat, M. Bekmezci, R. Darabi et al., Application of quasihexagonal Pt@PdS₂-MWCNT catalyst with high electrochemical performance for electro-oxidation of methanol, 2-propanol, and glycerol alcohols for fuel cells. *Mol. Catal.* **536**, 112874 (2023). <https://doi.org/10.1016/j.mcat.2022.112874>
 32. Z. Hu, Z. Wu, C. Han, J. He, Z. Ni et al., Two-dimensional transition metal dichalcogenides: interface and defect engineering. *Chem. Soc. Rev.* **47**(9), 3100–3128 (2018). <https://doi.org/10.1039/c8cs00024g>
 33. J. Zhang, T. Wang, D. Pohl, B. Rellinghaus, R. Dong et al., Interface engineering of MoS₂/Ni₃S₂ heterostructures for highly enhanced electrochemical overall-water-splitting activity. *Angew. Chem. Int. Ed.* **55**(23), 6702–6707 (2016). <https://doi.org/10.1002/anie.201602237>
 34. K. Chu, Y.-P. Liu, Y.-B. Li, Y.-L. Guo, Y. Tian, Two-dimensional (2D)/2D interface engineering of a MoS₂/C₃N₄ heterostructure for promoted electrocatalytic nitrogen fixation. *ACS Appl. Mater. Interfaces* **12**(6), 7081–7090 (2020). <https://doi.org/10.1021/acsami.9b18263>
 35. J. Szanyi, J.H. Kwak, R.J. Chimentao, C.H.F. Peden, Effect of H₂O on the adsorption of NO₂ on γ -Al₂O₃: an *in situ* FTIR/MS study. *J. Phys. Chem. C* **111**(6), 2661–2669 (2007). <https://doi.org/10.1021/jp066326x>



36. T. Venkov, K. Hadjiivanov, D. Klissurski, IR spectroscopy study of NO adsorption and NO + O₂ co-adsorption on Al₂O₃. *Phys. Chem. Chem. Phys.* **4**(11), 2443–2448 (2002). <https://doi.org/10.1039/b111396h>
37. T. Li, S. Han, Y. Wang, J. Zhou, B. Zhang et al., A spectroscopic study on nitrogen electrooxidation to nitrate. *Angew. Chem. Int. Ed.* **62**(19), e202217411 (2023). <https://doi.org/10.1002/anie.202217411>
38. P. Miró, M. Ghorbani-Asl, T. Heine, Two dimensional materials beyond MoS₂: noble-transition-metal dichalcogenides. *Angew. Chem. Int. Ed.* **53**(11), 3015–3018 (2014). <https://doi.org/10.1002/anie.201309280>
39. X. Zhang, G. Su, J. Lu, W. Yang, W. Zhuang et al., Centimeter-scale few-layer PdS₂: fabrication and physical properties. *ACS Appl. Mater. Interfaces* **13**(36), 43063–43074 (2021). <https://doi.org/10.1021/acsmi.1c11824>
40. A. Taherkhani, S.Z. Mortazavi, S. Ahmadi, A. Reyhani, Synchrotron EXAFS spectroscopy and density functional theory studies of Pd/MoS₂ Schottky-type nano/hetero-junctions. *Appl. Surf. Sci.* **604**, 154557 (2022). <https://doi.org/10.1016/j.apsusc.2022.154557>
41. M. Xiang, L. He, Q. Su, B. Sun, N. Wang et al., Supercapacitor properties of N/S/O Co-doped and hydrothermally sculpted porous carbon cloth in pH-universal aqueous electrolytes: mechanism of performance enhancement. *Chem. Eng. J.* **485**, 149835 (2024). <https://doi.org/10.1016/j.cej.2024.149835>
42. J. Liu, S.C. Smith, Y. Gu, L. Kou, C–N coupling enabled by N–N bond breaking for electrochemical urea production. *Adv. Funct. Mater.* **33**(47), 2305894 (2023). <https://doi.org/10.1002/adfm.202305894>
43. C. Dai, Y. Sun, G. Chen, A.C. Fisher, Z.J. Xu, Electrochemical oxidation of nitrogen towards direct nitrate production on spinel oxides. *Angew. Chem. Int. Ed.* **59**(24), 9418–9422 (2020). <https://doi.org/10.1002/anie.202002923>
44. H. Liao, T. Luo, P. Tan, K. Chen, L. Lu et al., Unveiling role of sulfate ion in nickel-iron (oxy)hydroxide with enhanced oxygen-evolving performance. *Adv. Funct. Mater.* **31**(38), 2102772 (2021). <https://doi.org/10.1002/adfm.202102772>
45. Q. Chen, Q. Zhang, B. Chen, J. Zhang, W. Peng et al., Enhanced long-term performance of sulfides in oxygen evolution reaction by sulfate ion-assisted strategy. *Adv. Funct. Mater.* **34**(44), 2406233 (2024). <https://doi.org/10.1002/adfm.202406233>
46. M. Kuang, Y. Wang, W. Fang, H. Tan, M. Chen et al., Efficient nitrate synthesis *via* ambient nitrogen oxidation with Ru-doped TiO₂/RuO₂ electrocatalysts. *Adv. Mater.* **32**(26), 2002189 (2020). <https://doi.org/10.1002/adma.202002189>
47. M. Anand, C.S. Abraham, J.K. Nørskov, Electrochemical oxidation of molecular nitrogen to nitric acid—towards a molecular level understanding of the challenges. *Chem. Sci.* **12**(18), 6442–6448 (2021). <https://doi.org/10.1039/D1SC00752A>
48. C.E. Hamilton, J.R. Lomeda, Z. Sun, J.M. Tour, A.R. Barron, Radical addition of perfluorinated alkyl iodides to multi-layered graphene and single-walled carbon nanotubes. *Nano Res.* **3**(2), 138–145 (2010). <https://doi.org/10.1007/s12274-010-1007-3>
49. Y. Cai, J. Li, L. Yi, X. Yan, J. Li, Fabricating superhydrophobic and oleophobic surface with silica nanoparticles modified by silanes and environment-friendly fluorinated chemicals. *Appl. Surf. Sci.* **450**, 102–111 (2018). <https://doi.org/10.1016/j.apsusc.2018.04.186>
50. G. Yu, J. Wang, H. Ma, X. Liu, S. Qin et al., Exploring abundantly synergic effects of K-Cu supported paper catalysts using TiO₂-ZrO₂ mesoporous fibers as matrix towards soot efficient oxidation. *Chem. Eng. J.* **417**, 128111 (2021). <https://doi.org/10.1016/j.cej.2020.128111>
51. H. Che, J. Wang, X. Gao, J. Chen, P. Wang et al., Regulating directional transfer of electrons on polymeric g-C₃N₅ for highly efficient photocatalytic H₂O₂ production. *J. Colloid Interface Sci.* **627**, 739–748 (2022). <https://doi.org/10.1016/j.jcis.2022.07.080>
52. D. Wang, W. Gong, J. Zhang, G. Wang, H. Zhang et al., *In situ* growth of MOFs on Ni(OH)₂ for efficient electrocatalytic oxidation of 5-hydroxymethylfurfural. *Chem. Commun.* **57**(86), 11358–11361 (2021). <https://doi.org/10.1039/D1CC04680B>
53. H. Wang, G. Yan, M. Li, H. Ji, Y. Feng et al., Nucleophilic ring-opening of thiolactones: a facile method for sulfhydrylization of a carbon nanotube-based cathode toward high-performance Li–S batteries. *ACS Sustain. Chem. Eng.* **10**(15), 5005–5014 (2022). <https://doi.org/10.1021/acssuschemeng.2c00204>
54. F. Luo, P. Yu, J. Xiang, J. Jiang, S. Chen, *In situ* generation of oxyanions-decorated cobalt(nickel) oxyhydroxide catalyst with high corrosion resistance for stable and efficient seawater oxidation. *J. Energy Chem.* **94**, 508–516 (2024). <https://doi.org/10.1016/j.jechem.2024.03.006>
55. G. Liu, L. Ding, Y. Meng, A. Ali, G. Zuo et al., A review on ultra-small undoped MoS₂ as advanced catalysts for renewable fuel production. *Carbon Energy* **6**(2), e521 (2024). <https://doi.org/10.1002/cey2.521>
56. S. Liu, X. Zhang, S. Wu, X. Chen, X. Yang et al., Crepe cake structured layered double hydroxide/sulfur/graphene as a positive electrode material for Li-S batteries. *ACS Nano* **14**(7), 8220–8231 (2020). <https://doi.org/10.1021/acsnano.0c01694>

Publisher's Note Springer Nature remains neutral with regard to jurisdictional claims in published maps and institutional affiliations.